

A Semiempirical Modeling of Soil Moisture, Vegetation, and Surface Roughness Impact on CYGNSS Reflectometry Data

Simon H. Yueh^{ID}, *Fellow, IEEE*, Rashmi Shah^{ID}, *Senior Member, IEEE*, M. Julian Chaubell^{ID}, Akiko Hayashi, Xiaolan Xu^{ID}, *Member, IEEE*, and Andreas Colliander^{ID}, *Senior Member, IEEE*

Abstract—Data from the Cyclone Global Navigation Satellite System (CYGNSS) mission augmented with a physical surface scattering model were analyzed to develop a semiempirical model, which consists of three main modeling components for soil moisture, vegetation, and surface roughness. CYGNSS data collected from March 2017 to March 2020 were collocated with the soil moisture data from the Soil Moisture Active Passive (SMAP) mission and climatology vegetation water content (VWC) derived from the Moderate Resolution Imaging Spectroradiometer (MODIS) normalized difference vegetation index (NDVI) data. The matchup data were binned as a function of soil moisture, VWC, and incidence angle. The CYGNSS data were calibrated using a coherent reflection equation to obtain an effective reflectivity. The response of CYGNSS effective reflectivity to soil moisture changes is consistent with the change of the Fresnel reflectivity based on Mironov's soil dielectric constant model used by the SMAP and Soil Moisture Ocean Salinity (SMOS) missions for soil moisture retrieval. The CYGNSS effective reflectivity decreases approximately linearly (in dB) with respect to the NDVI-VWC. The estimated values of vegetation attenuation parameter (b) agree with values published in the literature and are corroborated with the estimated values of b using the SMAP dual-polarized channel algorithm based on land cover types. A CYGNSS surface scattering map has been derived and reveals a mixed contribution of coherent and incoherent scattering effects and the effects of topography. The semiempirical model, leveraging two of the key modeling functions used by microwave radiometry, will pave the way for a synergistic use of reflectometry and radiometry data for multiparameter retrieval and development of consistent soil moisture products.

Index Terms—Bistatic radar, reflectivity, signals of opportunity, soil moisture.

I. INTRODUCTION

SOIL moisture is an important component of the water cycle. Accurate information on global soil moisture is critical for land surface hydrogeology modeling and, hence, weather and hydrologic forecasts. The Soil Moisture Active Passive (SMAP) [1] and Soil Moisture Ocean Salinity (SMOS)

Manuscript received April 4, 2020; revised September 1, 2020 and October 3, 2020; accepted October 7, 2020. Date of publication November 26, 2020; date of current version December 2, 2021. (Corresponding author: Simon H. Yueh.)

The authors are with Jet Propulsion Laboratory, California Institute of Technology, Pasadena, CA 91109 USA (e-mail: simon.yueh@jpl.nasa.gov; rashmi.shah@jpl.nasa.gov; mario.j.chaubell@jpl.nasa.gov; akiko.k.hayashi@jpl.nasa.gov; xiaolan.xu@jpl.nasa.gov; andreas.colliander@jpl.nasa.gov).

Digital Object Identifier 10.1109/TGRS.2020.3035989

missions [2] have already been providing new insight into near-surface soil moisture storage using the L-band radiometry at a spatial resolution of 30–50 km. The SMAP data from ascending and descending passes allow a revisit of every one to two days, depending on latitude.

Global Navigation Satellite System (GNSS) Reflectometry (GNSS-R), offering a new data source for land surface soil moisture, was initially developed for ocean altimetry [3], [4] and has been extended to land remote sensing [5]–[9]. The advancements in GNSS-R technologies led to the selection of the Cyclone GNSS (CYGNSS) mission by the National Aeronautics Space Administration (NASA) [10]. The theoretical principle of inferring soil moisture from GNSS-R data is based on the response of L-band microwave reflectivity to surface soil moisture [5]. Airborne measurements have demonstrated the proof of concept during several field campaigns [6]–[9]. The use of GNSS-R data for crop growth monitoring [8] and vegetation biomass retrieval [11] has also been demonstrated. Further demonstration of spaceborne GNSS reflectivity dependence on surface soil moisture was shown based on the TechDemoSat-1 (TDS-1) data in [12]–[14]. However, due to the limited data records from TDS-1 and a lack of compensation for surface scattering effects, the correlation analysis [13] was generally noisy and insufficient to allow an accurate determination of soil moisture and vegetation impact.

Recently, several empirical approaches for soil moisture retrieval from CYGNSS data have been published based on the collocations of CYGNSS data and SMAP soil moisture retrieval by using a linear regression [15]–[18] and an artificial neural network trained with the *in situ* station data [19]. Al-Khalidi *et al.* [20] introduced a time-series approach using the minimum and maximum of the bistatic radar cross sections (BRCSs) derived from the CYGNSS data along with the corresponding SMAP soil moisture to retrieve the soil moisture from each CYGNSS observation in a time window. It assumes that the surface reflection can be modeled by geometric optics (GO) scattering; hence, the impact of soil moisture can be captured by the Fresnel reflectivity, and the vegetation attenuation can be canceled out by taking the ratio of successive CYGNSS BRCS measurements. In addition, Carreno-Luengo *et al.* [21] have performed a retrieval of biomass from the CYGNSS trailing edge width and reflectivity

by an empirical correlation with the Above Ground Biomass (AGB) products from the Geoscience Laser Altimeter System (GLAS) instrument onboard the Ice, Cloud, and land Elevation Satellite.

To gain physical insights, electromagnetic modeling analyses have been performed to examine the relationship of GNSS-R signals to vegetation and forest canopies [22]–[26]. Theoretical models are known to be valuable for the diagnosis of physical scattering mechanisms but are often impractical for a direct application to satellite data due to the requirement of a large number of modeling parameters.

We are, therefore, motivated to develop a semiempirical model, which builds on the functional form of physical models, but with a limited set of coefficients derivable from data. It incorporates the Mironov dielectric constant model [27] of soil used for the modeling of passive microwave brightness temperatures by SMAP and SMOS. This allows the nonlinear relationship between data and soil moisture, as well as texture to be considered more effective than linear regressions [15]–[18]. The vegetation attenuation is also related to a model used by passive microwave radiometry with a linear dependence on the vegetation water content (VWC). On the effects of surface roughness scattering, we introduce a bulk surface scattering factor, which can also be estimated from the data. The semiempirical model, leveraging two of the key modeling functions used by microwave radiometry, will pave the way for a synergistic use of reflectometry and radiometry data for multiparameter retrieval and also the development of consistent soil moisture products.

In this article, in Section II, we present analyses on the theoretical impact of surface roughness and vegetation to help establish the functional form of the semiempirical model. The collocation of CYGNSS and SMAP data and signature analyses of CYGNSS data are described in Section III. The results of global CYGNSS and SMAP correlation analysis to relate the CYGNSS reflectivity data to soil moisture, VWC, and surface roughness are described in Section IV. Results of analyses based on land cover types are presented in Section V. A summary of our findings is given in Section VI.

II. CYGNSS RADIOMETRIC MODELING AND EFFECTIVE REFLECTIVITY

A. Radiometric Calibration

The CYGNSS reflectometry measurement geometry is illustrated in Fig. 1. The algorithm for calibration of CYGNSS data can be found in [28]. The GNSS signals scattered near the specular direction include coherent reflection and incoherent scattering by rough surfaces [29]–[32]. The total power (P_r^S) is the sum of coherent and incoherent components, denoted by P_c and P_i , respectively

$$P_r^S = P_c + P_i \quad (1)$$

They can be represented in the specular direction for the coherent reflection by

$$P_c = \Gamma(\theta) \frac{\lambda^2 P_t G_t G_r}{(4\pi)^2 (R_t + R_r)^2} \quad (2)$$

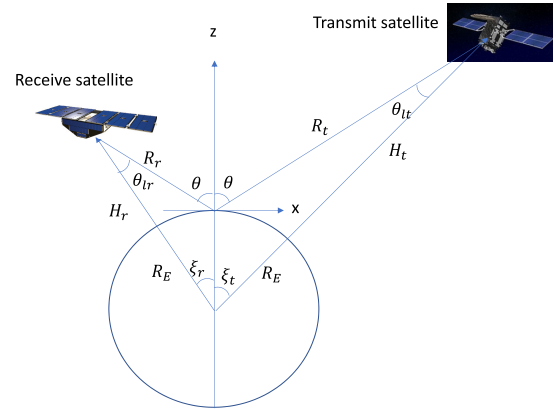


Fig. 1. Measurement geometry for GNSS-R. The CYGNSS' orbit altitude (H_r) is nominally between 510 and 530 km, while the GPS satellite is positioned much higher at 202 000 km (H_t).

and the incoherent scattering by the bistatic radar equation [31]

$$P_i = \frac{\lambda^2 P_t G_t}{(4\pi)^3} \int \frac{G_r}{R_t^2 R_r^2} \sigma_s \chi^2(\tau, f_D) dA \quad (3)$$

where $P_t G_t$ is the global positioning system (GPS) equivalent isotropically radiated power (EIRP), which is inferred from the direct measurements by CYGNSS; G_r is the antenna gain toward the specular point; R_t is the distance between the GPS transmitter and specular point; R_r is the distance between the CYGNSS receiver and specular point; $\Gamma(\theta)$ is the coherent reflectivity at the angle of incidence (θ); λ is the GPS wavelength (19 cm); σ_s is the incoherent normalized radar cross section of rough surfaces and vegetation; and χ^2 is the Woodward ambiguity function (WAF), which can be found in [31]

$$\chi^2(\tau, f_D) \approx \Lambda^2(\tau) \text{sinc}^2(f_D T_i) \quad (4)$$

where τ is the excess time delay with respect to the specular point, f_D is the Doppler shift, $T_i = 1$ ms is the integration time for CYGNSS, and the square of the autocorrelation of GPS signal can be expressed as [20]

$$\Lambda^2(\tau) = \left(1 - \frac{|\tau|}{\tau_c} \right)^2 \quad (5)$$

if $|\tau| < \tau_c$ and 0 otherwise. τ_c is one chip length, corresponding to 293 m.

For the radiometric calibration of CYGNSS data, we estimate the noise-free power by performing a noise subtraction.

$$\tilde{P}_r^S = P_r - P_N \quad (6)$$

where P_r is the power of the CYGNSS L1 delay Doppler map (DDM) at the direction of the specular point (center of DDM). The noise power (P_N) is estimated from the first two Doppler bins in the DDM assuming they are far from the peak. If the peak exists in these first two Doppler bins, which happens when topography is not well accounted for in the delay-Doppler computation model, the CYGNSS data are ignored.

In the CYGNSS Level 1 data release, the raw counts have been calibrated into analog power and BRCS by using

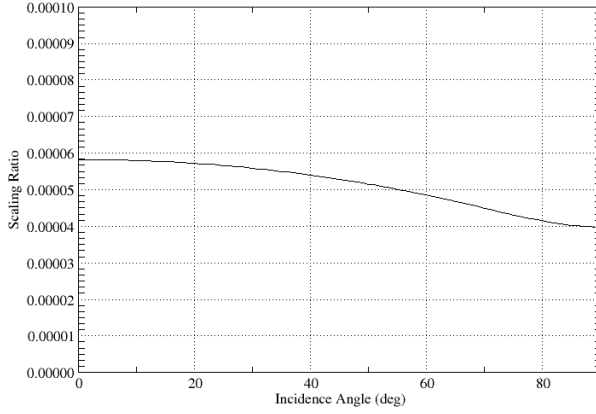


Fig. 2. Scaling factor (S) for diffused bistatic scattering coefficients.

instrument noise levels, atmospheric loss, and blackbody load noise and temperature estimates [28]. The BRCS calibration is similar to what has been done for nominal spaceborne monostatic (backscatter) radar missions. However, for CYGNSS, we cannot obtain a range-free calibrated BRCS because it is not possible to partition of the CYGNSS data into coherent and incoherent components that have a different range dependence based on (2) and (3). Since we cannot estimate the coherent reflectivity and incoherent bistatic BRCS independently, we chose to estimate an effective reflectivity based on the inversion of (2)

$$\Gamma_{\text{eff}}(\theta) = \frac{\tilde{P}_r^S(4\pi)^2(R_t + R_r)^2}{\lambda^2 P_t G_t G_r} \quad (7)$$

Assuming the spatial variations of σ_s , distances to the footprint and receiver gain are negligible over the region of integration, and the effective reflectivity can be expressed as

$$\Gamma_{\text{eff}}(\theta) = \Gamma(\theta) + \sigma_s S \quad (8)$$

where S , the weighting factor for the incoherent radar cross section, is related to the distances from GPS and CYGNSS satellites to the specular point

$$S = \frac{A_{\text{eff}}(R_t + R_r)^2}{4\pi R_t^2 R_r^2} \quad (9)$$

with the effective area related to the WAF

$$A_{\text{eff}} = \int \chi^2(\tau, f_D) dA \quad (10)$$

For aircraft- and tower-based systems, located at low altitudes ($R_r \sim 10$ m – 10 km), the scaling factor S can be rather large, in the order of 0.1–10, allowing the incoherent scattering coefficients to make a significant contribution. The scaling factor will reduce with increasing receiver altitude and can become quite small for spaceborne systems with a large R_r . Fig. 2 illustrates the amplitude of S versus incidence angle for CYGNSS and GPS altitudes. Its amplitude is in the range of 0.00005–0.00006 for an incidence angle of 60° or smaller.

Please note that the CYGNSS data have been calibrated into the BRCS using the bistatic radar equation [28]. However, the resulting BRCS will contain a term related to the coherent reflectivity weighted by a range dependent factor. Regardless

of the calibration method, the analog power, effective reflectivity, and BRCS all have equivalent information and can be converted into the others.

B. Surface Roughness Effects

In general, the terrain surfaces within 20–30 km enclosed by one chip length of GPS are spatially heterogeneous and can have multiple spatial scales from meters (plots and fields) to kilometers (hills and mountains). In this section, we provide examples based on the scattering from a well-established surface scattering model, the Kirchhoff approximation (KA), to illustrate general signatures and relative significance of coherent and incoherent surface scattering at the forward direction to help interpret the CYGNSS data. It is not our objective to fit the CYGNSS data with KA modeling. Instead, our objective is to find a functional representation of the semiempirical model that allows the estimation of net surface scattering effects.

Under the KA, sometimes denoted as physical optics, for rough surface scattering [29]–[32], the electromagnetic fields at any location on the surfaces can be approximated by the fields on a tangent plane. In other words, the curvature of the surfaces at any location has a radius much larger than the electromagnetic wavelength. The scattered fields (E) recorded by the GNSS-R receivers include coherent reflection and incoherent scattering in the specular direction. It is nominally assumed under the KA that the surface roughness can be characterized by the Gaussian statistics with a standard deviation for the rms height and a spatial correlation function. The coherent field is then the expected value of the scattered field, $\langle E \rangle$, while the incoherent component is the random component, $E - \langle E \rangle$, with its power described by $\langle |E|^2 \rangle - |\langle E \rangle|^2$. The angular brackets denote the ensemble average.

Along the specular direction, the coherent term can be expressed as [29]

$$\Gamma(\theta) = \alpha |R|^2 \quad (11)$$

where R is the Fresnel reflection coefficient and α , denoted as scattering loss, accounts for the loss of coherent power due to diffused scattering

$$\alpha = e^{-4k^2 h^2 \cos^2 \theta} \quad (12)$$

where k is the electromagnetic wavenumber, and h is the root-mean-square (rms) surface height.

The KA further suggests that the incoherent term near the specular direction has the same dependence as that of the coherent term on the Fresnel reflectivity [29], [32]

$$s_{00} \cong f_s(\text{roughness}, \theta) |R|^2. \quad (13)$$

The expression of the incoherent BRCS can be found for a Gaussian correlation function in [29], [30], and [32] and an exponential correlation in [32]. It is unlikely that the surface roughness within tens of km of the one-chip length covered by CYGNSS can be characterized by a single correlation function. The KA results can only serve as a benchmark. However, it is known that the multiplicative form described by (13) is applicable to several physical surface scattering mechanisms,

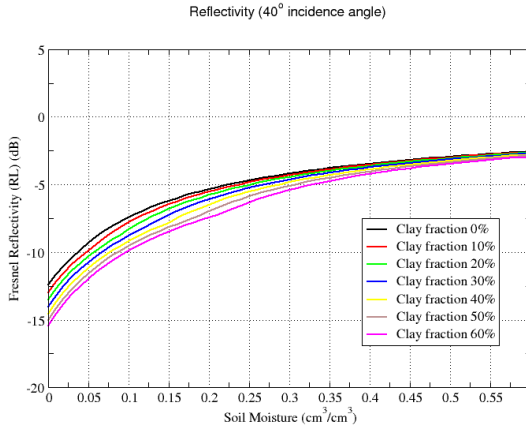


Fig. 3. Fresnel reflectivity for RHCP transmit and LHCP receive versus soil moisture for a range of clay content based on the Mironov dielectric model.

including the GO and KA [29]–[32]. Hence, (13) is generally applicable over a broad range of surface roughness conditions.

Substituting (13) into (8) allows the effective reflectivity to be represented by the sum of Fresnel reflectivity reduced by the scattering loss (α) and the incoherent scattering weighted by the scaling factor (S)

$$\Gamma_{\text{eff}}(\theta) = [\alpha + f_s S] |R|^2. \quad (14)$$

Here, it is shown that the effects of surface roughness and soil moisture can be approximately separated. The soil moisture information is in $|R|^2$ alone. We will later use the CYGNSS data to confirm the linear relationship of the effective reflectivity to the square of the Fresnel reflection coefficient $|R|^2$.

The relative contributions of coherent reflection (α) and incoherent scattering ($f_s S$) depend on the surface roughness, which influences the amplitudes of the two terms in the brackets. As the surface roughness increases, the scattering loss, the first term in the bracket, will reduce exponentially, while the incoherent term will also decrease and become more diffused over a wider range of angles.

In the following, examples are provided to illustrate the characteristics of coherent reflection and incoherent scattering terms at the CYGNSS orbit altitude in order to assess their relative amplitude and dependence on the incidence angle.

Fig. 3 illustrates the Fresnel reflectivity for right-hand-circular-polarization (RHCP) transmit and left-hand-circulation-polarization (LHCP) receive versus soil moisture based on the Mironov dielectric model [27] for a range of clay fraction at an incidence angle of 40°, which is the incidence angle used by SMAP. The Mironov model has been used by the SMAP and SMOS passive microwave missions for soil moisture retrieval. There are other soil moisture dielectric models, but the Mironov model is generally considered as the most advanced model by the community up to this point, hence chosen by the two space missions for data processing. As indicated in Fig. 3, the Fresnel reflectivity changes by about 3.5 dB for an increase of soil moisture from 0.1 to 0.4 m³/m³ for low clay fraction, and the changes can reach 6 dB for high clay fraction. The characteristics are similar at other incidence angles. In any case, the shape of curves is nonlinear, deviating from the linear regression model described in [15]–[18].

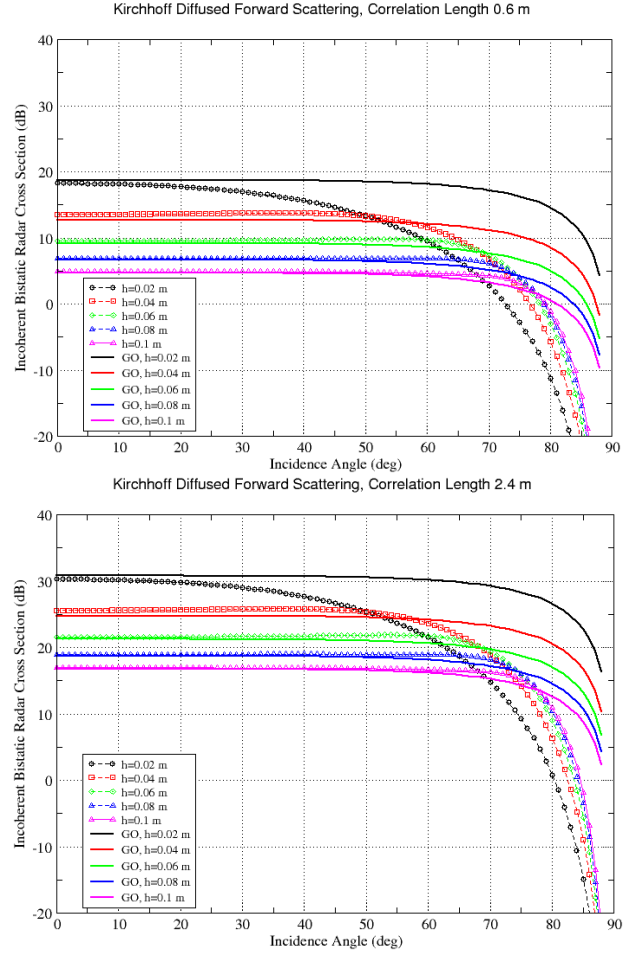


Fig. 4. Bistatic normalized radar cross section in the specular direction for a soil moisture value of 0.3 m³/m³ and a clay fraction of 0.4 for a range of surface roughness values. Upper figure: 0.6 m for correlation length; lower figure: 2.4 m for correlation length. The curves with symbols are evaluated using the KA (dashed lines with symbols). The curves without symbols are based on the GO approximation.

Without loss of generality, we will use a Gaussian correlation function to indicate the impact of surface roughness on the incoherent bistatic scattering coefficients and, hence, effective reflectivity. We can evaluate the incoherent scattering term (σ_{s0}) based on the KA for given soil moisture, rms roughness (h), and correlation length (l) using the equations described in [29, pp. 82 and 83]. As an example, Fig. 4 illustrates the incoherent reflection for two correlation lengths, 0.6 and 2.4 m, and an rms roughness in the range of 2–10 cm. As the surface roughness increases, the incoherent bistatic normalized radar cross section decreases. For comparison, also included in the charts are the GO approximation (solid curves) with the normalized radar cross section related to the rms slope of surfaces (s^2)

$$\sigma_{s0GO} \cong \frac{|R|^2}{s^2} \quad (15)$$

where, for the Gaussian correlation [29], [32], the rms slope is

$$s^2 = \frac{h^2}{4l^2} \quad (16)$$

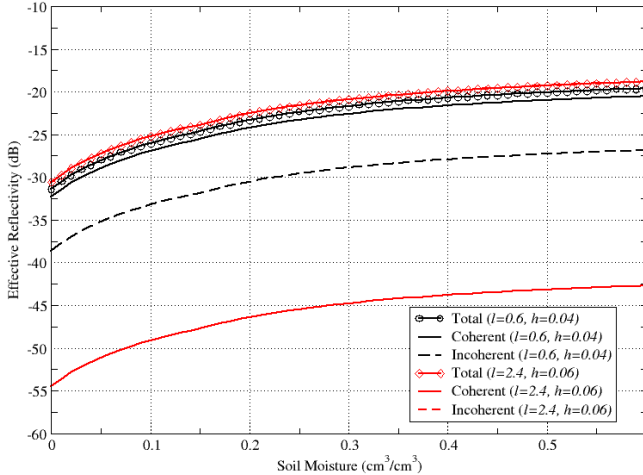


Fig. 5. Total, coherent, and incoherent scattering all have essentially the same response to soil moisture under the KA at an incidence angle of 40°. Two cases are illustrated. The total effective reflectivity of the two cases is very close, but the relative contributions of coherent and incoherent terms are different. Coherent reflection dominates for the case with $l = 0.6$ and $h = 0.04$, while incoherent scattering dominates for $l = 2.4$ and $h = 0.06$. The units of correlation length and rms roughness, indicated in the legends, are in meters. The analysis uses a clay fraction of 0.4.

As shown in Fig. 4, σ_{s0} of GO is close to that of KA for small incidence angles and large rms slopes. Comparing the upper and lower figures with results for two distinct correlation lengths, we can find that a higher correlation length (lower figure) results in a larger incoherent scattering in the specular direction. The magnitude of changes is approximately proportional to l^2 , essentially signified by the expression of GO approximation [see (15) and (16)]. The difference of 12 dB is substantial between the results for the two correlation lengths, 0.6 and 2.4 m.

We selected two sets of roughness parameters among those cases illustrated in Fig. 4 to illustrate the soil moisture dependence of the effective reflectivity along with its coherent and incoherent components at an incidence angle of 40° in Fig. 5. The first case has a correlation length of 0.6 m and an rms roughness of 4 cm, while the second case has a correlation length of 2.4 m and an rms roughness of 6 cm. The total and individual components have essentially the same soil moisture response (other than an offset) as implied by the KA or GO discussed earlier. Although the total effective reflectivity for these two cases is essentially the same over the entire range of soil moisture, the relative contributions of coherent and incoherent terms are very different.

For case 1 with $h = 4$ cm and $l = 0.6$ m (black curves), the coherent term is larger than the incoherent term by more than 7 dB (see Fig. 5). For soil moisture of 0.3 m³/m³, σ_{s0} is close to 13 dB (see Fig. 4), and hence, the scaling factor (S) of 0.000055 (see Fig. 2) leads to an incoherent effective reflectivity of about -29 dB. For the coherent term, the Fresnel reflectivity is quite large, about -6 dB for soil moisture of 0.3 m³/m³; however, the surface scattering loss (α) of about -17 dB reduces the coherent term to a magnitude of slightly lower than -22 dB, which is still 7 dB larger than the incoherent term.

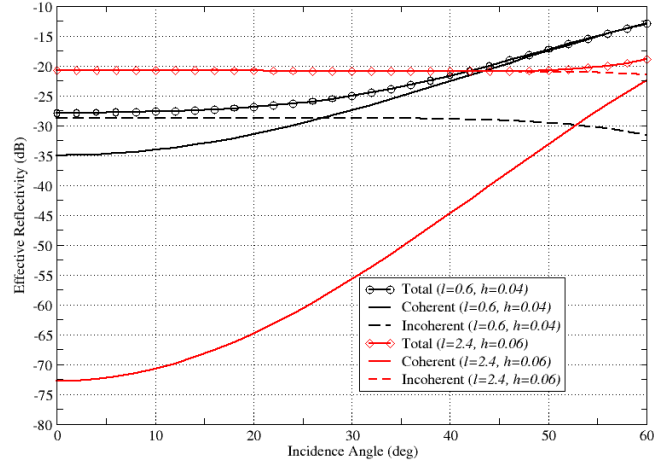


Fig. 6. Effective reflectivity and its components for soil moisture of 0.3 m³/m³ and a clay fraction of 0.2 are illustrated as a function of incidence angle. The values of roughness parameters are the same as in the cases illustrated in Fig. 5. For $l = 0.6$ and $h = 0.04$, the total effective reflectivity rises by 15 dB from 0 to 60°, whereas, for $l = 2.4$ and $h = 0.06$, the total effective reflectivity is essentially unchanged. The correlation length and roughness are in meters.

For case 2 with $h = 6$ cm and $l = 2.4$ m illustrated in Fig. 5, the incoherent term dominates, and the contribution of the coherent term is negligible due to the large diffused scattering loss or a very small α (-40 dB). The incoherent reflection σ_{s0} is very large, close to 22 dB (see Fig. 4). After a reduction by the weighting factor S , the incoherent component of effective reflectivity remains quite high with an amplitude close to -21 dB for soil moisture of 0.3 m³/m³.

The numerical examples illustrated in Fig. 5 support the functional form described in (14) with all scattering components exhibiting the same dependence on soil moisture.

However, the characteristics of these two cases can be differentiated by comparing their incidence angle dependence (see Fig. 6) although their effective reflectivity is essentially indistinguishable at the incidence angle of 40° (see Fig. 5). For case 1, the effective reflectivity has a strong angular dependence with its value increased by 15 dB from nadir viewing to an incidence angle of 60° (see Fig. 6). The large change in magnitude, essentially contributed by the coherent term, is due to a reduced $\cos^2\theta$ for increasing incidence angle and, hence, an increase in α at high incidence angles. In contrast, the effective reflectivity essentially has no incidence angle dependence for case 2 due to a smaller contribution from the coherent term. A dominant diffused scattering for case 2 leads to a small dependence on the incidence angle.

C. Semiempirical Model and Vegetation Effects

Vegetation can introduce an attenuation on the surface scattering [13], [21], [23], [26] and a volume scattering by various vegetation components [22]–[25]. Note that the volume scattering by vegetation will also be subject to the weighting by the WAF due to the autocorrelation of GPS signal and Doppler filtering. Since we chose the center of DDM for analysis, the contribution of volume scattering will be limited to within one chip length based on (5). Therefore, the semiempirical

model of CYGNSS effective reflectivity is described in the following with the impact of vegetation modeled by a two-way attenuation on the surface scattering and introduction of an incoherent volume scattering term contributed by vegetation

$$\Gamma_{\text{eff}}(\theta) = e^{-2\tau} [\alpha + f_s S] |R|^2 + \gamma_v S \quad (17)$$

where τ is the one-way attenuation and γ_v is the incoherent bistatic normalized radar cross section of vegetation. The same scaling factor (S) has to be applied to the incoherent volume scattering by vegetation due to the fact that the incoherent volume scattering term will have to be included in the integral of (3) to compute the incoherent power.

This functional form differs from that proposed in [13], which has introduced an additional attenuation effect by the albedo of vegetation on the first term, but has not included the volume scattering term. At this point, we do not have reliable ancillary vegetation albedo data globally to quantify the impact of albedo. It is neglected for now but should be considered for a future extension when accurate albedo data become available.

Note that the volume scattering by vegetation is essentially incoherent as long as the vertical distribution of vegetation elements is more than 1/4 wavelength, which will cause a phase variation from 0° to 360° for scattering by vegetation elements at different depths; this, consequently, will reduce the coherent component of volume scattering by vegetation. For short vegetation with a height of under 1/4 wavelength, a coherent term might be required.

For passive microwave soil moisture missions, such as SMAP, it has been assumed that τ can be related to VWC linearly [33], [35]

$$\tau = \frac{b \cdot \text{VWC}}{\cos\theta} \quad (18)$$

The values of b reported in [35] were in the range of 0.05–0.2 for a few crops but could reach 0.7 for tall grass at L-band frequencies. For SMAP, a static global gridded map of b based on land cover types has been used. One of the key questions that remain to be addressed is whether this linear model is applicable to reflectometry.

The magnitude of γ_v for corn ($\text{VWC} < 3 \text{ kg/m}^2$) can be found in [24] based on the simulation by a coherent scattering model [25] to account for the scattering from corn stalks, leaves, and cobs. The simulated γ_v , varying with incidence angles, has a peak value near -12 dB around 20° – 30° of incidence and reduces to about -23 dB at an incidence angle of 10° and 70° . After accounting for the scaling factor (S), the contribution of volume scattering from corn to the effective reflectivity will be -50 dB or lower, which is much smaller than the coherent surface reflection or incoherent scattering based on Figs. 5 and 6 and also apparently much smaller than the nominal CYGNSS effectiveness reflectivity (see Fig. 7). The contribution of volume scattering by corn to the effective reflectivity and other crops is expected to be negligible for CYGNSS.

The simulation of volume scattering from Aspen forests with a much higher VWC and biomass based on a bistatic radiative transfer model can be found in [22], which shows

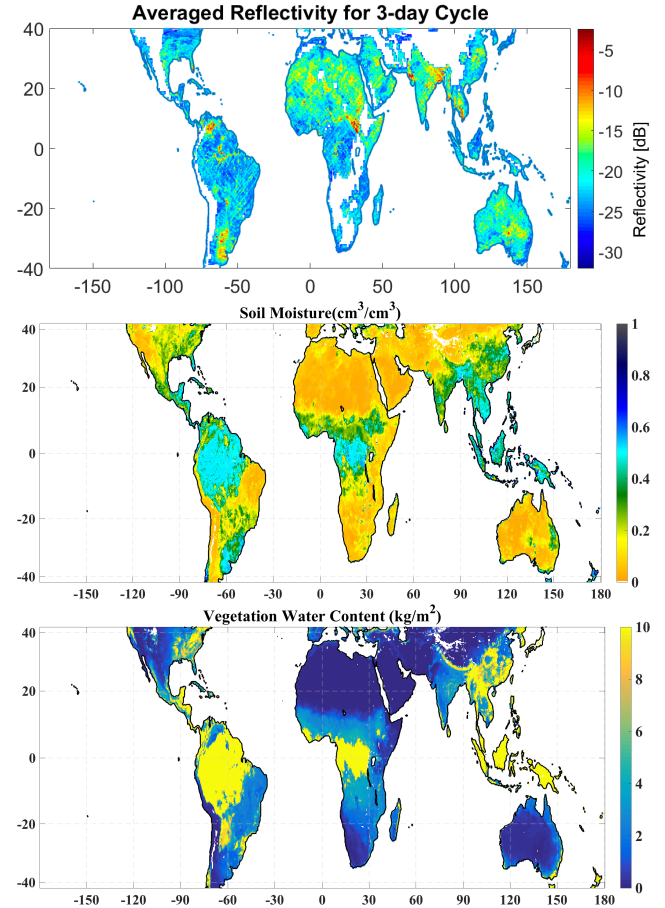


Fig. 7. Three-day composite images of CYGNSS effective reflectivity (top), SMAP soil moisture (middle), and NDVI-derived VWC (bottom) for September 30–October 2, 2017.

that the normalized radar cross sections of Aspen trunks can vary between 6 and 11 dB over a range of incidence angles and can increase with trunk heights to reach 12 dB for a height of 12 m. The corresponding effective reflectivity of Aspen forests for CYGNSS would be from -36.5 to -30.5 dB after accounting for the scaling factor ($S = 0.000055$ or -42.6 dB). This suggests that the volume scattering by forests with a higher density and larger trunks than Aspen forests could remain small but not negligible.

If the vegetation layer can be represented by a cloud of discrete scatterers uniformly distributed within the thickness (H_t), then the normalized radar cross section can be integrated over the thickness:

$$\gamma_v = \int_0^{H_t} \rho \sigma_0 e^{-2\mu z} dz \quad (19)$$

where ρ is the number of scatterers per unit volume, σ_0 is the radar cross section of each scatterer, and μ is the attenuation per unit length. It is straightforward to carry out the integration and recast the vegetation volume scattering effectively in the following form:

$$\gamma_v = \gamma_{v0} (1 - e^{-2\tau}) \quad (20)$$

where γ_{v0} is the normalized radar cross section for an infinite vegetation height. More sophisticated vegetation scattering models can be found in [22]–[25].

A few key observations can be made from the semiempirical relationship described in (17) if the vegetation volume scattering (γ_v) is negligible, i.e., much smaller than the surface scattering.

- 1) The effective reflectivity is proportional to the Fresnel reflectivity $|R|^2$, which is related to soil moisture, regardless of the relative contribution of coherent and incoherent terms. This supports the regression approaches published in [15]–[18] as long as the surface roughness and vegetation attenuation at the location of interests do not vary over the time window of interests.
- 2) The effective reflectivity will be proportional to the two-way attenuation by vegetation [19], [21]. Taking a logarithm of the effective reflectivity can separate the effects of vegetation attenuation and surface scattering. This supports the method indicated in [20], which takes the ratio of two subsequent CYGNSS BRCSSs to isolate the effect of soil moisture.

However, if there is a substantial amount of vegetation, the surface scattering could be significantly attenuated, and the effective reflectivity could still be impacted by the volume scattering of vegetation γ_v .

III. CYGNSS AND SMAP MATCHUP DATA

The CYGNSS V2.1 Level 1 data acquired from March 2017 to March 2020 were collocated with the SMAP soil moisture product based on the Single Channel Algorithm for Vertically (SCA-V) polarized brightness temperatures [33], as well as the soil moisture and vegetation optical depth (VOD) from the Dual-Channel Algorithm (DCA) with both vertical and horizontal polarizations [34]. The SMAP data are gridded on the 9-km EASE-2 grid.

The VWC climatology derived from the Moderate Resolution Imaging Spectroradiometer (MODIS) normalized difference vegetation index (NDVI), which is used as ancillary data for SMAP soil moisture retrieval, was also obtained from the SMAP product grid. For each CYGNSS data, SMAP data within 25 km in spacing and closest in time within one day are included in the matchups.

Fig. 7 illustrates a three-day composite of CYGNSS Γ_{eff} , SMAP soil moisture, and VWC. In most parts of Australia, Sahara, and Saudi Arabia, where soil moisture and VWC were both low, the CYGNSS effective reflectivity was relatively high, in the range of -15 to -20 dB, only about a few dB lower than the Fresnel reflectivity for dry soil ($<0.05 \text{ m}^3/\text{m}^3$) (see Fig. 3). Since the VWC was low over these regions, the difference from the Fresnel reflectivity is essentially due to the surface scattering loss (α); if the coherent reflection dominates, the corresponding rms surface roughness (h) would be about 2 cm based on (12), which will lead to a value of about -4.4 dB for α . The corresponding value of $H = 4k^2h^2$ will be 1.74. The value of H used in the passive microwave radiative transfer model, which also uses the same equation e^{-H} to correct surface reflectivity, is about 0.1 to 0.2 for SMAP [33], much smaller than the values ($H = 4k^2h^2$) suggested by the CYGNSS data. This highlights a key difference between passive and active microwave techniques.

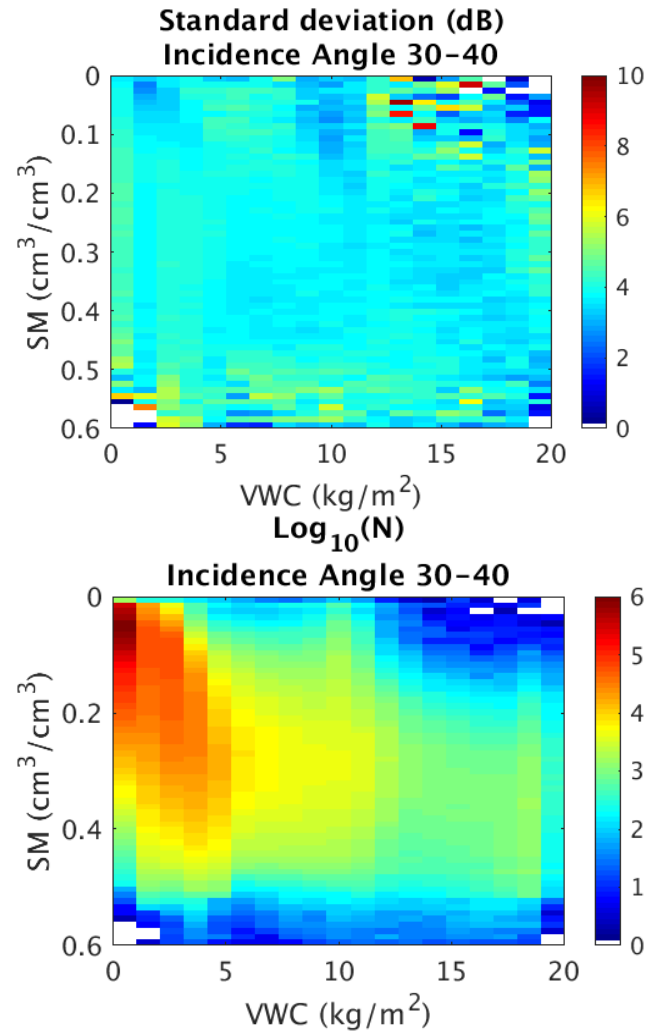


Fig. 8. Statistics of the matchup for data in the range of incidence angles from 30° to 40° . The standard deviation of effective reflectivity in each bin (top). Number of matchups in each bin (bottom).

Passive microwave reflectivity is the integration of bistatic scattering coefficients (coherent and incoherent) over the upper hemisphere [29], not the same as the value of Γ in the specular direction. They become the same only if the surface is flat (no diffused scattering). The impact of surface roughness on active microwave radar and reflectometer is much larger than that on passive microwave radiometry. Directly using the value of passive microwave H from SMAP for CYGNSS bistatic radar roughness modeling is inappropriate in general.

For regions with a high VWC ($>8 \text{ kg/m}^2$) indicated by yellow in Fig. 7, such as Amazon, Congo, Southeast Asia, and U.S. east coast with dense and mixed forests, the CYGNSS effective reflectivity could be -25 dB or lower. In comparison with the Fresnel reflectivity of about -5 dB for soil moisture of 0.3, the reduction is about 20 dB or more. The large reduction in magnitude with respect to the Fresnel reflectivity suggests the impact of vegetation attenuation (τ) and/or scattering loss (α) due to rough surfaces, while the additional contribution by vegetation volume scattering (γ_v) to the effective reflectivity remains to be relatively weak (<-30 dB)

and is insufficient to offset the reduction in coherent surface reflection and incoherent scattering.

IV. GLOBAL ENSEMBLE STATISTICS

We binned the CYGNSS effective reflectivity as a function of SMAP soil moisture, VWC, and incidence angle at a step of 1% in soil moisture and 1 kg/m² in VWC for every 10° in incidence angle. We computed the average and standard deviation of the collocated data in each bin. The numbers of collocations and standard deviation are illustrated in Fig. 8 for the CYGNSS angle of incidence in the range of 30° to 40°. The matchup statistics are similar in the other ranges of incidence angles (not shown). The standard deviation accounts for the variation of surface roughness, temporal and spatial mismatches, and errors in the calibration of CYGNSS effective reflectivity, SMAP soil moisture, and NDVI-VWC climatology. We find that the value of standard deviation is nominally about 4 dB, which is most likely due to the variability of surface roughness for collocated data in a given soil moisture-VWC bin from various locations; this will be justified in Section V based on the analysis of surface scattering in the CYGNSS data.

As shown in Figs. 4–6, surface roughness can impact the coherent reflection and incoherent scattering easily by 10 dB or more and can contribute to the standard deviation of the data from different locations collocated in the same bin. However, given a large number of collocations in each bin for three years of CYGNSS data, the uncertainty of the averaged effective reflectivity will be much smaller. We can find that in the lower figure of Fig. 8, the number of matchups for many bins is about 1000 or more. Assuming that the uncertainties are fully random for each pair of matchups, the uncertainty of the bin average would be about $4/\sqrt{N} = 0.13$ dB for $N = 1000$ or 0.4 dB for $N = 100$ (high soil moisture or VWC).

We have illustrated the average of CYGNSS reflectivity in each bin versus the SMAP SCA-V soil moisture in Fig. 9. Overall, the data in adjacent soil moisture bins in Fig. 9 do not go up and down by much. The smoothness of curves in Fig. 9 indicates a small random uncertainty of the averaged data in each bin. In general, the effective reflectivity increases with increasing soil moisture, except for the bins with soil moisture greater than 0.5, which have much fewer samples (tens to a few hundred), as indicated in the lower figure of Fig. 8. We find that the characteristics and levels of effective reflectivity are similar across the six ranges of incidence angles. Several key features are described in the following.

A. Soil Moisture Dependence

To begin with, let us examine the soil moisture dependence of data in the lowest VWC bin (0–1 kg/m²) in the incidence angle range of 30°–40° to determine whether the sensitivity to soil moisture can be characterized by the Fresnel reflection coefficients based on the Mironov dielectric constant model [27]. As the soil moisture increases from 0.1 to 0.4, the increase in the CYGNSS reflectivity is about 5 dB, very close to the changes indicated in Figs. 3 and 5. The theoretical reflectivity based on the Mironov dielectric model

was performed with the results overlaid with the CYGNSS data. The agreement is excellent for soil moisture in the range of 0.1–0.5 cm³/cm³ for all incidence angles (see Fig. 10). Please note that a constant offset of 16 dB, likely due to surface roughness impact, was added to the CYGNSS data to reduce the bias.

The systematic offset between the averaged CYGNSS effective reflectivity and Mironov's model for low soil moisture (<0.1 cm³/cm³) shown in Fig. 10 could possibly be due to a bias in the probability distribution of surface roughness. The data for many regions with low soil moisture may tend to have a smoother surface with an rms height smaller than 4 cm, leading to a smaller scattering loss (α) and, hence, a higher effective reflectivity or incoherent scattering. As discussed earlier, the surface roughness of the dry regions (see Fig. 7), including many parts of Sahara, Middle East, and Western Australia, could be near 2 cm on average, much smaller than the value of 4 and 6 cm used for the model simulation (see Fig. 5). (Note that there are regions with complex topography in these dry regions, but they represent a minor population in the overall collocations.) Therefore, the CYGNSS effective reflectivity may level off to about –8 dB for all incidence angles (see Fig. 10) for the VWC bin in the range of 0–1 kg/m², rather than falling further to –13 dB or lower for reduced soil moisture (<0.05 cm³/cm³). Regardless, the consistency over the soil moisture range of 0.1–0.5 supports the use of Mironov's soil dielectric constant model [27] to model the response of CYGNSS effective reflectivity (coherent or incoherent) to soil moisture.

B. Impact of Surface Roughness

The second feature concerns the impact of scattering loss by surface roughness. The effective reflectivity for soil moisture of 0.3 cm³/cm³ at an incidence angle of 30°–40° is about –20 dB (see Fig. 9), which is close to the values of the two cases illustrated in Fig. 5 with the rms heights being 4 and 6 cm, respectively. An rms height of 5 cm would lead to a large scattering loss due to diffused scattering. The resulting value of $H = 4k^2h^2$ for reflectometry will be 10.8, much larger than the value of H (0.1–0.2) used for soil moisture retrieval from the L-band passive microwave brightness temperatures [33], which also uses the same functional form e^{-H} to reduce the surface reflectivity. The roughness parameter values (H) for passive microwave radiometry are too small for the modeling of reflectometry.

C. Dependence on Vegetation Water Content

The final feature concerns the influence of vegetation. A comparison of the data in ten VWC bins illustrated in Fig. 9 reveals that the sensitivity of effective reflectivity to soil moisture reduces with increasing VWC. The dependence of CYGNSS reflectivity on VWC is directly indicated in Fig. 11 for nine ranges of soil moisture. The characteristics are similar for all six incidence angle ranges. The vertical spreading of nine curves in each figure is due to the soil moisture dependence. The spreading reduces with increasing VWC, indicating the growing impact of VWC, similar to what

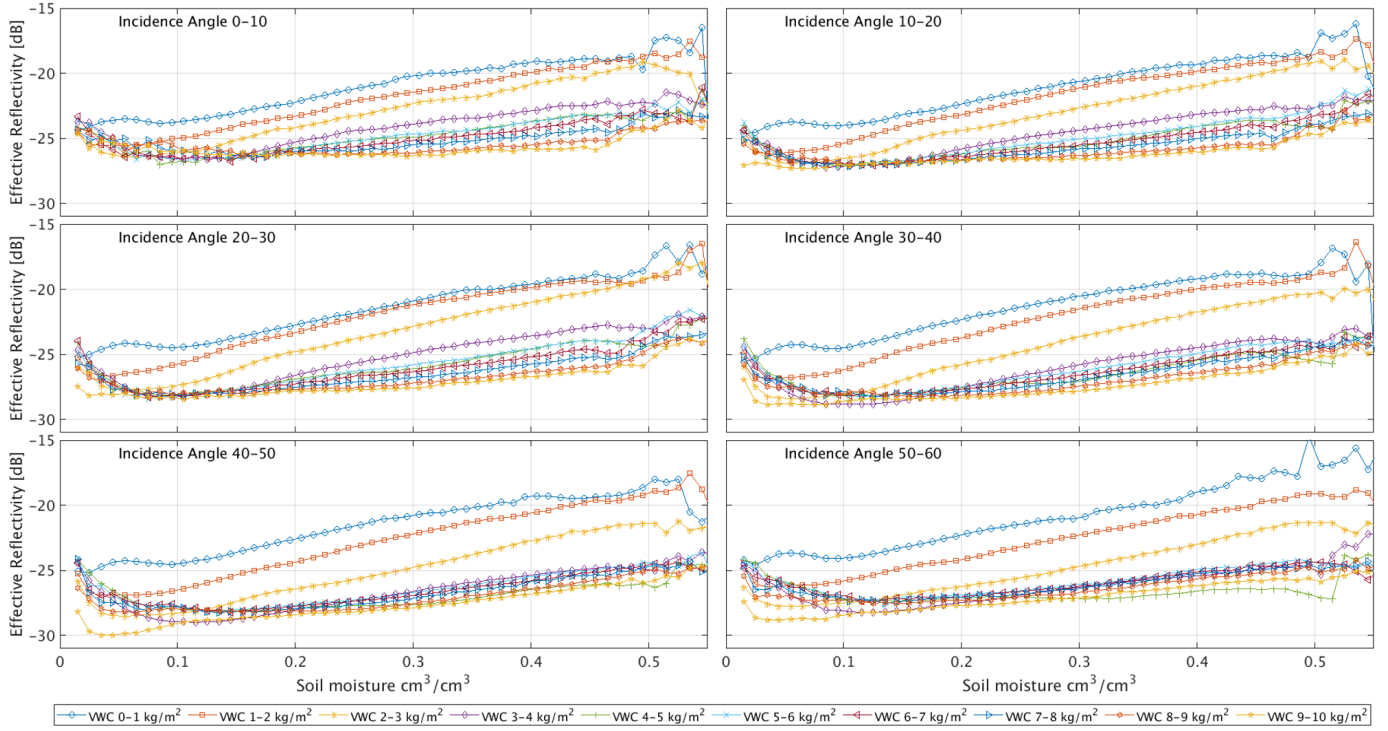


Fig. 9. CYGNSS reflectivity versus SMAP soil moisture for ten ranges of VWCs. Each figure corresponds to the data over a range of incidence angles at 10° steps. An increase in reflectivity corresponds to an increase in soil moisture, except the data with soil moisture >0.5. The reflectivity data for the lowest VWC bin (0–1 kg/m²) have the highest value. Data for higher VWCs reveal lower reflectivity.

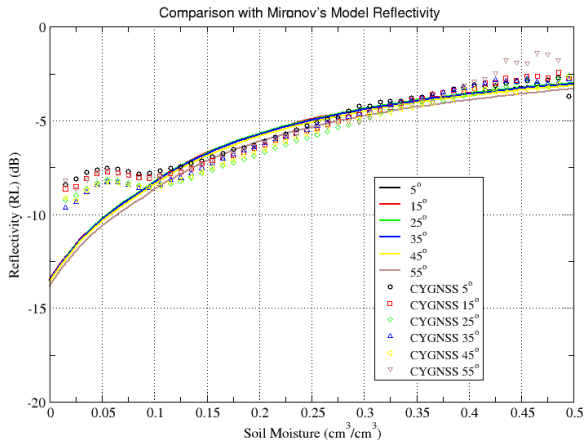


Fig. 10. Theoretical reflectivity (solid curves) computed based on the Mironov's dielectric constant model using clay fraction = 0.2 at six incidence angles from 5° to 55° and overlaid with the CYGNSS effective reflectivity (symbols) for VWC < 1 kg/m². The 16-dB positive bias is added to the CYGNSS reflectivity to reduce the gap.

is presented in Fig. 9. As the VWC reaches about 18 kg/m², the curves for various soil moistures appear to essentially converge. At that point, soil moisture retrieval using the effective reflectivity at the peak of DDM is not possible.

Fig. 11 suggests that the decreasing trend can be approximately represented by two linear segments with different slopes, below and above a VWC of about 5 kg/m². This is most evident in the three higher incidence angle figures (>30° in incidence). For VWC values under about 5 kg/m²,

the decreasing trend is steeper than that for a higher VWC. It should be noted that the data from the lower and higher VWC values are mostly from different geographical regions (see Fig. 7). The higher VWC regime (>5 kg/m²) includes several regions: U.S. east coast, central America, southeast Asia, Congo, and Amazon, with mixed and dense forests.

To isolate the effects of vegetation attenuation, we need to exclude the contribution by vegetation scattering. For high biomass and VWC, woody forests are expected to have a high volume scattering [22] and attenuation [21], [23], i.e., $\gamma_v \approx \gamma_{v0}$. According to (20), the rough surface contribution to the effective reflectivity to the first order can be estimated as

$$\Gamma_{\text{eff}}(\theta) - \gamma_{v0}S \cong e^{-2\tau}[(\alpha + f_s S)|R|^2]. \quad (21)$$

The right-hand side of the equation is a product of two terms: vegetation attenuation and surface reflection in the brackets. They can be separated by taking the logarithm of the estimated surface reflectivity on the left-hand side of the equation.

The value of γ_{v0} should be slightly lower than the value of effective reflectivity at the point of convergence of multiple curves (see Fig. 11) because there could be some residual contribution by surface scattering. Fig. 12 illustrates the estimated contribution by surface scattering [left-hand side of (21)]. For the high VWC range (>5 kg/m²), a value of -30.5 dB for $\gamma_{v0}S$ (or 7.7 dB for γ_{v0}) was applied. No subtraction ($\gamma_{v0} = 0$) was made to the data for the lower VWC range (<5 kg/m²).

The choice of -30.5 dB is within the possible range of volume scattering by trees in view of the theoretical model simulations for Aspen forests [22]. As discussed earlier, the

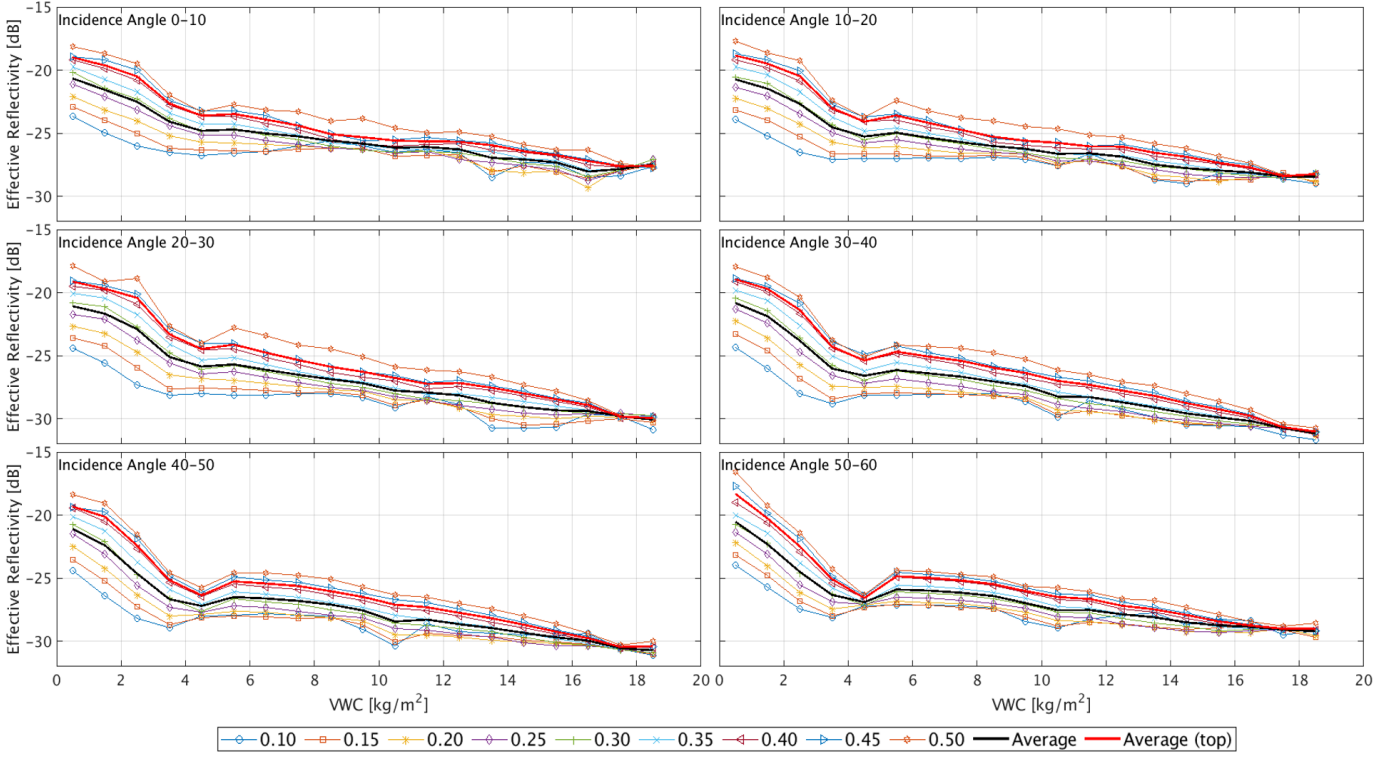


Fig. 11. Reflectivity versus VWC from 0 to 18 kg/m². There are nine curves in each figure for soil moisture between 0.1 and 0.5 m³/m² at 0.05 steps with legends indicated above. The black solid line corresponds to the average of data in nine soil moisture bins, while the red solid curve the average of data in the top four soil moisture levels (0.35–0.5 m³/m²).

theoretical effective reflectivity of Aspen tree trunks can be as high as -30.5 dB for 12-m trees after accounting for the scaling factor ($S = 0.000055$) and turns out to be close to the lower bound of the effective reflectivity shown in Fig. 11. The value of $\gamma_{v0}S$ for other types of forests with a higher density and larger trunks can be larger.

For crops, the biomass and VWC are much lower than those of woody vegetation. The magnitude of γ_v for volume scattering from corns (VWC < 3 kg/m²) can be found in [24] based on the simulation by a coherent scattering model [25] and can be as high as -12 dB, leading to a value of -55 dB for $\gamma_{v0}S$, which is much smaller than the lower bound of effective reflectivity illustrated in Fig. 11; hence, it can be justified that there is no need to correct the volume scattering by crops or other grassy vegetation for the CYGNSS effective reflectivity.

After the correction of volume scattering with an approximate value indicated above, we find that the curves for different soil moisture in Fig. 12 become more parallel to each other for VWC under 15 kg/m². In other words, the VWC dependence of effective reflectivity for different soil moisture becomes more consistent. In addition, the dip and kink in the CYGNSS effective reflectivity near the VWC of 5 kg/m², most notably in the red curves in Fig. 11, have been much reduced (see Fig. 12).

We have varied the values of $\gamma_{v0}S$ by plus and minus one dB for the correction of effective reflectivity for VWC > 5 kg/m², and the nearly parallel features shown in Fig. 12 essentially stay the same. This supports the feasibility to separate the vegetation attenuation and surface scattering to

the zeroth-order. The quasi-linear dependence of effective reflectivity on VWC (see Fig. 12) supports the use of a linear model [see (18)] to parameterize the vegetation attenuation. Note that the NDVI-derived VWC may not be accurate for high VWCs. The observed quasi-linear dependence is conditioned on the characteristics of the NDVI-derived VWC.

We have applied a linear regression to the data illustrated in Fig. 12 for three VWC ranges: below or above 5 kg/m² and all together for given soil moisture. There are nine soil moisture ranges at each incidence angle for each VWC range. The error bars are computed as the standard deviation of the nine estimates conditioned on each soil moisture range. The mean values and error bars are illustrated in Fig. 13 versus the incidence angle. The slopes could be slightly different below and above 5 kg/m² and, however, are pretty much within the error bars of each other.

The estimated slopes indicate that the CYGNSS effective reflectivity can reduce by 1 dB for every 1-kg/m² change in VWC at low incidence angles and about 1.5 dB for every 1-kg/m² change at high incidence angles (see Fig. 13). The observed sensitivity to VWC is substantial.

The estimated regression slopes (see Fig. 13) can be used to estimate the value of “ b ” by using (18). The values of b estimated from three VWC ranges again are close together. The estimated value from the CYGNSS data is in reasonable agreement with the value of $b = 0.12$ estimated based on a much more limited TDS-1 data [13] and is within the range of experimental values from 0.05 to 0.2 [35].

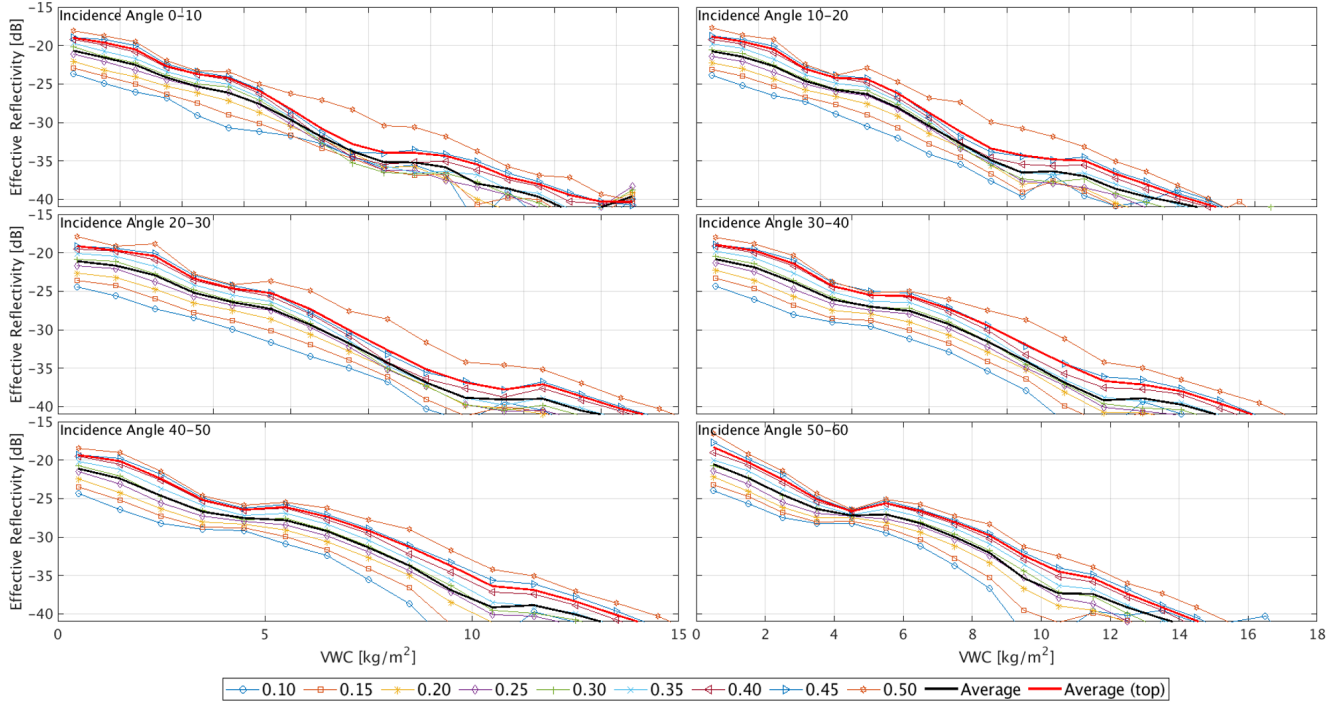


Fig. 12. Reflectivity versus VWC from 0 to 15 kg/m². There are nine curves in each figure for soil moisture between 0.1 and 0.5 m³/m² at a step of 0.05 m³/m² with legends indicated above. The black solid line corresponds to the average of data in nine soil moisture bins, while the red solid curve is the average of data in the top four soil moisture levels (0.35–0.5 m³/m²). Black and red soil curves are nearly parallel to each other, suggesting a negligible influence by any residual CYGNSS receiver noise after calibration. The applied correction is $\gamma_{v0} = -30.5$ dB for VWC > 5 kg/m² and 0 for VWC < 5 kg/m².

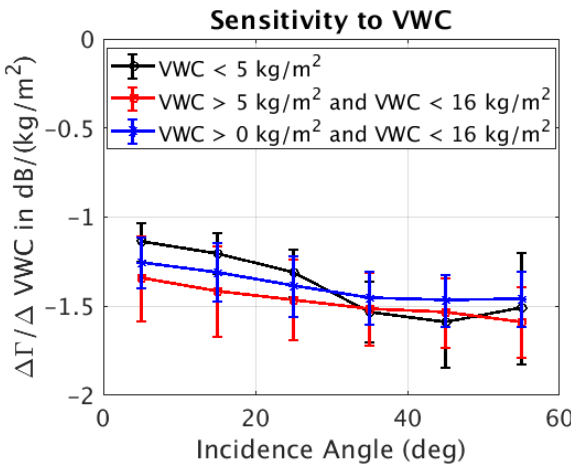


Fig. 13. Slopes of the linear regression of reflectivity against VWC increase with incidence angle for VWC < 5 kg/m², but stay roughly level for higher VWCs.

The resulting estimations of “*b*” are illustrated versus the incidence angle (see Fig. 14). There is a dependence on the incidence angle. This observation of incidence angle dependence differs from the nominal assumption used for the L-band passive microwave radiometry retrieval of soil moisture that “*b*” is independent of incidence angles. The CYGNSS data suggest a necessity to account for the orientation of vegetation components for microwave attenuation by vegetation for reflectrometry.

We can fit the incidence angle (θ) dependence of the *b* parameter estimated using the full range of VWC by a cubic

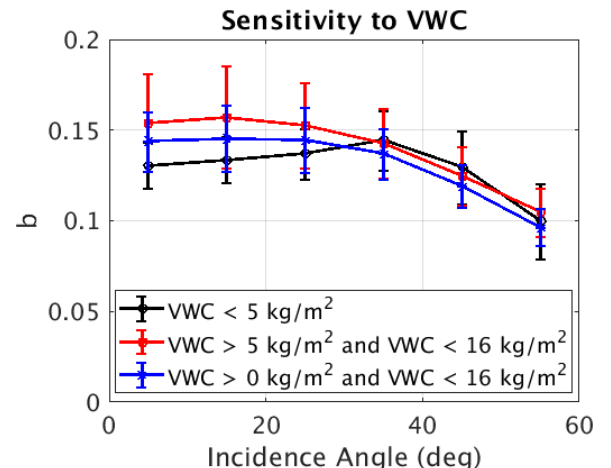


Fig. 14. Estimated value of *b* as a function of incidence angle.

polynomial, which is given in the following:

$$b = 0.141 + 0.0006424\theta - 1.448 \cdot 10^{-5}\theta^2 - 2.17 \cdot 10^{-7}\theta^3. \quad (22)$$

It is critical to recognize that this empirical equation based on a global analysis cannot account for spatial variability. For our analysis, the vegetation modeling coefficients, *b* and its angular behavior (see Fig. 14), are “ensemble average” of the data within the CYGNSS coverage. We can expect that there should be regional dependence. For example, Jackson *et al.* [35] have shown that the value of *b* does depend on the types of crops and grass.

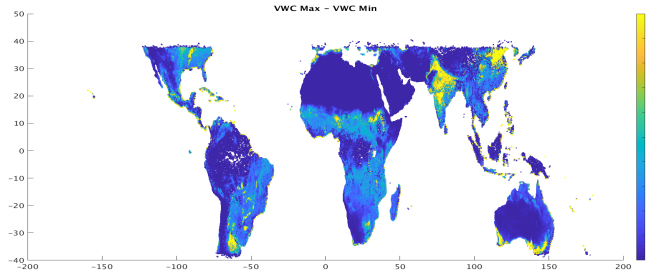


Fig. 15. Range of NDVI-VWC climatology within the CYGNSS coverage. The unit of the color key is kg/m^2 .

V. ANALYSIS BY LAND COVER TYPES

The regional dependence could be addressed by a correlative analysis of the data binned on each SMAP Equal-Area Scalable Earth-2 (EASE-2) grid. However, the temporal variability of VWC is small ($<1 \text{ kg}/\text{m}^2$) for most locations (see Fig. 15), except the regions with significant agriculture activities, such as the United States Midwest, Argentina pampas, northern India, and southeast of Australia. A small VWC range makes it impractical to accurately estimate the value of b at each location.

We, therefore, divided the CYGNSS coverage into five regions with color coding of the International Geosphere–Biosphere Programme (IGBP) land cover type inside each region (see Fig. 16). The data were then analyzed based on the land cover type within each of the five regions. We performed a linear regression of the effective reflectivity against the VWC. The estimated values of b from the CYGNSS effective reflectivity are in reasonable agreement with the estimates from the SMAP DCA [34] (see Fig. 16 and Table I). A specific region with a large difference between CYGNSS and SMAP DCA estimates of b is the evergreen forested region in Congo (row 2, IGBP class 2 in Fig. 16), where the CYGNSS effective reflectivity shows essentially no dependence on VWC. The CYGNSS estimate for Congo, inconsistent with other regions, could be caused by errors in the SMAP SCA-V soil moisture or NDCI-VWC matchup over Congo. This requires further investigation.

The other region with a large discrepancy is the IGBP barren land cover. The value derived from the SMAP DCA is much larger than expected and could possibly be due to the error in the surface roughness parameter (H) values for the SMAP VOD retrieval.

Table I provides a side-by-side comparison of the SMAP DCA and CYGNSS b values after averaging over five regions for each land cover type. The scatter plot is illustrated in Fig. 17, indicating a correlation coefficient of 0.745 and an rms difference of 0.028.

The values of b for open shrublands are consistent with the results shown in [33]. It is interesting to note that, for evergreen broadleaf forests, the values of b of both CYGNSS and SMAP DCA are close to 0.05, a factor of three smaller than that of open shrublands. The smaller than expected values for evergreen and deciduous broadleaf forests have

TABLE I
COMPARISON OF SMAP DCA AND CYGNSS b VALUES. THE EVERGREEN BROADLEAF IN CONGO FOR CYGNSS IS EXCLUDED FROM AVERAGING. IF IT IS INCLUDED, THE CYGNSS b WOULD BE 0.037

Land Cover Type	SMAP DCA b	CYGNSS b
2. Evergreen Broadleaf	0.050	0.045
4. Deciduous Broadleaf	0.065	0.071
5. Mixed Forest	0.064	0.054
6. Closed Shrub	0.090	0.109
7. Open Shrub	0.169	0.166
8. Woody Savannas	0.078	0.037
9. Savannas	0.079	0.125
10. Grassland	0.134	0.088
12. Croplands	0.082	0.055
14. Crops and vegetation	0.078	0.050
16. Barren	0.310	0.025

been suggested by the theoretical predictions based on a numerical solution technique for the scattering from a cluster of cylinders [36].

Our results for broadleaf and evergreen forests are complementary to the findings in [21], which shows the attenuation of CYGNSS “reflectivity” due to the AGB of tropical forests. It should be noted that the biomass of vegetation represents the dry mass of vegetation, while the VWC is the wet part of vegetation mass. However, it is conceivable that there could be a correlation between them. In any case, [21, Fig. 5] does not indicate an obvious “lower bound” of the CYGNSS “reflectivity” over the Amazon and Congo forests and suggests a substantial penetration to the forest floor. Our analyses based on the correlation with VWC appears to be consistent with the analysis presented in [21] based on the correlation with biomass, suggesting that the L-band microwave signals from reflectometry and radiometry can penetrate various forest canopies (see Table I).

The final step of our semiempirical modeling analysis is to quantify the surface roughness impact. The effects of surface roughness will be modeled by a “bulk” surface scattering parameter (AFS), which can be estimated to the first order by inverting it from (17)

$$\text{AFS} = \alpha + f_s S = \frac{\Gamma_{\text{eff}}(\theta) - \gamma_{v0} S}{e^{-2\tau} |R|^2} \quad (23)$$

where τ is computed using (18) with the NDVI-VWC as the input and the estimated values of b . The Fresnel reflection coefficient (R) is computed using the Mironov dielectric constant with the SMAP SCA-V soil moisture as the input. We let γ_{v0} to be -30.5 dB for $\text{VWC} > 5 \text{ kg}/\text{m}^2$ and 0 otherwise.

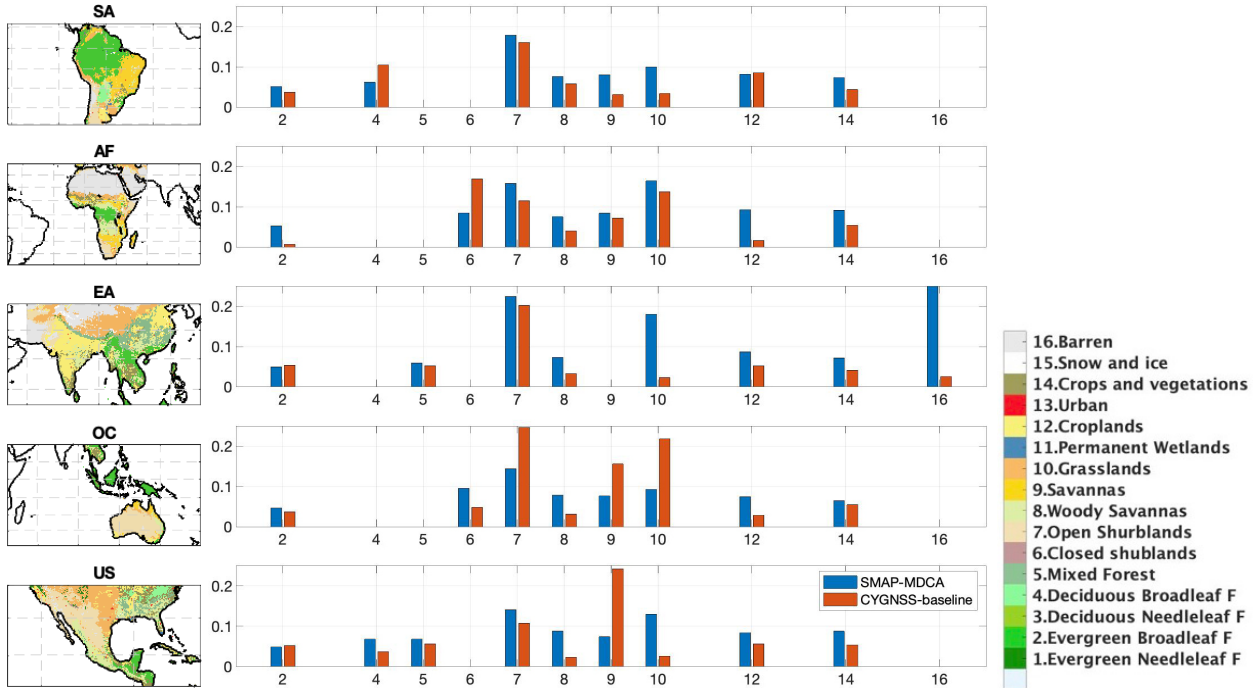


Fig. 16. Five figures are color-coded land cover types for five regions within the CYGNSS coverage. The estimated values of b for each land cover type. Red bars for CYGNSS-derived estimates. Blue bars for the SMAP-DCA algorithm.

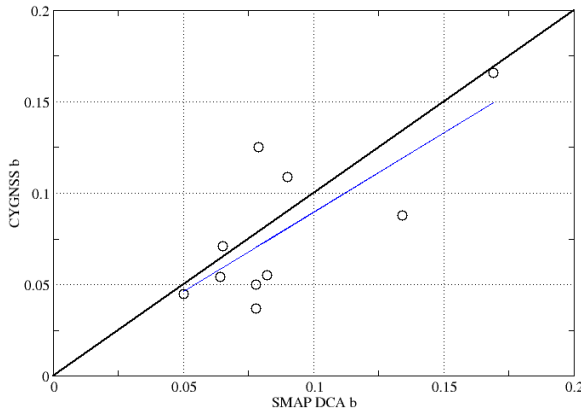


Fig. 17. CYGNSS versus SMAP DCA b for each land cover type. The circles are data. The solid black line is the diagonal line, while the blue line is the linear regression of CYGNSS versus SMAP. The data for the barren surface are excluded. The standard deviation of difference is 0.028. The correlation coefficient of regression is 0.745.

Under the assumption that the surface scattering effect is static, the values of AFS in dB are accumulated and averaged at each SMAP EASE-2 grid based on the data from three years. The averaged AFS for data acquired from 35° to 45° in incidence angle is illustrated in Fig. 18. The high ends (>-13 dB) of AFS are mostly located over deserts and croplands. Areas with a complex topography (e.g., Rockies, Andes, Tibetan plateau, Ahaggar and Tibesti mountains in the Sahara, Hejaz and Asir mountains in the Arabia peninsula, and Macdonnell Ranges in Australia) have low values (<-18 dB). The regions surrounding many river channels in South America and Africa are visible with a high AFS. The values of AFS

clearly indicate the influence of topography, supporting our hypothesis that it is insufficient to model the surface scattering using small scale surface roughness alone.

We have derived the AFS maps for every 10° following the same procedures stated above and applied a linear regression to estimate the change of AFS versus incidence angle using the data with an incidence angle of larger than 30° at each location. The linear regression slope (dB/ $^{\circ}$) is illustrated in Fig. 19. The regions, color-coded in blue, have a negative slope, which is a characteristic of incoherent scattering.

However, a large portion of land surfaces is color-coded in red (see Fig. 19), with a positive slope, suggesting that the contribution of coherent reflection could be noticeable at high incidence angles (see Fig. 6). Note that a slope of 0.05 (dB/ $^{\circ}$) corresponds to an increase of 1.5 dB for a change of incidence angle from 30° to 60° . The change of 1.5 dB is far smaller than the change of 12 dB shown in Fig. 6 for the case of $h = 4$ cm with a dominant coherent reflection but is closer to the case of $h = 6$ cm with a minor contribution from coherent reflection. Extra care on the incidence angle correction prior to the use of CYGNSS data for soil moisture retrieval suggested in [12] has to be considered: some regions (blue) require a positive correction, while some other regions (red) require a negative correction.

We have conducted an analysis of the variability of AFS for each land cover type. The data illustrated in Fig. 18 are grouped into land cover types. The mean and standard deviation (error bars) are illustrated in Fig. 20. The error bars in the range of 3–6 dB are consistent with the standard deviation of the binning illustrated in Fig. 8.

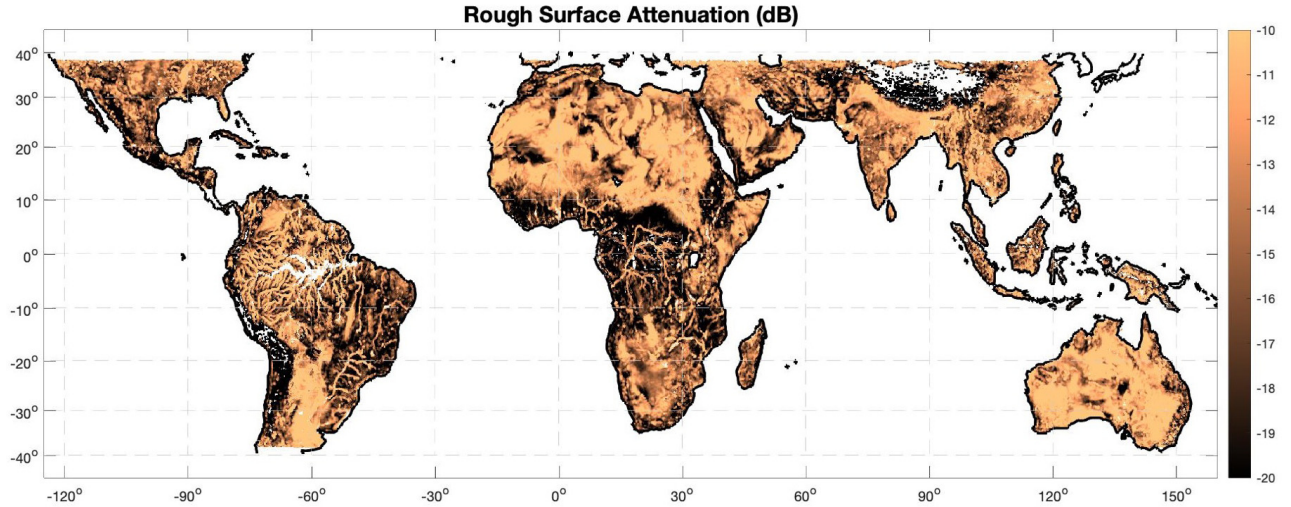


Fig. 18. Rough surface scattering term in dB at the incidence angle of 40°.

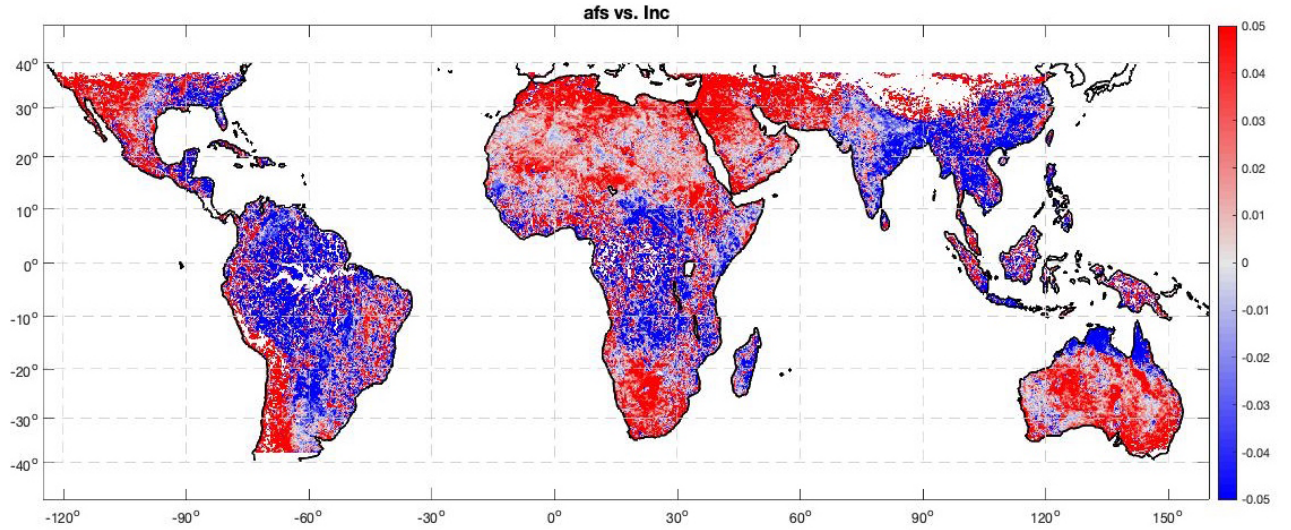


Fig. 19. Linear regression slope (dB/°) of the rough surface scattering term based on the data acquired in the incidence angle range of 30° to 60°. The slope is mostly smaller than 0.05 dB/°, which corresponds to an increase of the surface scattering by 1.5 dB from 30° to 60°. For regions with more tree canopies, the slope tends to be negative. A slope of -0.05 dB/° corresponds to a reduction of 1.5 dB from 30° to 60°.

The consistency supports the notion that the dominant error source to the binning for the global analysis presented in Section IV is due to the variability of surface roughness.

VI. SUMMARY

We have analyzed the CYGNSS data and explored the correlation of the data with the collocated SMAP soil moisture and NDVI-derived climatology VWC. A semi-empirical model, including the influence of surface reflection, vegetation attenuation, and volume scattering, was constructed with a limited number of modeling parameters. Through the comparative analysis of data and model, we have derived the model coefficients empirically by examining the dependence of the data on VWC and soil moisture.

It can be concluded that the soil moisture dependence of the CYGNSS reflectivity agrees well with the characteristics of the Fresnel reflectivity computed with the Mironov dielectric constant model, which has been used by the SMAP and SMOS missions for soil moisture retrieval from brightness temperatures.

The dependence of vegetation attenuation on VWC is approximately linear for VWC as high as 15 kg/m². The values of b estimated from the CYGNSS data are in good agreement with the historical experimental data record and the values derived from the SMAP dual-polarized brightness temperatures. The CYGNSS data also suggest the influence of volume scattering contribution by forests. The corresponding bistatic normalized radar cross section is about 12 or -31 dB , including the scaling factor, which could be due to the relatively large woody structure in forests as predicted by a physical scattering model [22].

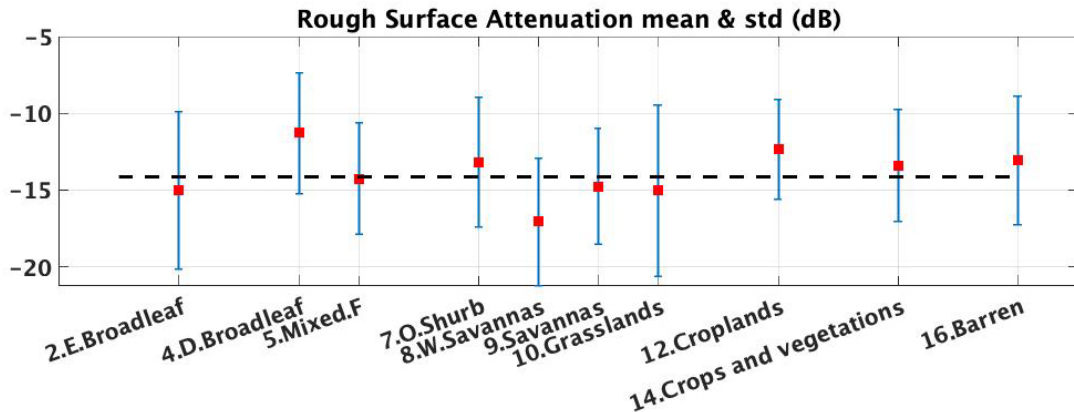


Fig. 20. Rough surface scattering illustrated in Fig. 18 is grouped into land cover types, and the mean and error bars corresponding to one standard deviation are plotted for each land cover type. One standard deviation is about 4 dB.

We have derived an effective surface scattering coefficient (AFS) at each location, which can account for the coherent and incoherent scattering for CYGNSS. The weak incidence angle dependence of the CYGNSS AFS suggests that the CYGNSS effective reflectivity is mostly dominated by incoherent surface scattering within the CYGNSS footprint although the coherent contribution is evident over many regions.

Our regression analysis has not explicitly accounted for the impact of biomass (dry mass of vegetation). As shown in [21], biomass is highly correlated with the microwave attenuation through tropical forests. Large woody structures can introduce significant microwave scattering and extinction. The results published in [11] and [21] clearly show that GNSS-R data depend on biomass for forest canopies. It is expected that the attenuation by dry biomass needs to be included together with the contribution by VWC to fully account for the total attenuation by trees for a semi-empirical model or any other models. The analysis of the joint impact of VWC and biomass is beyond the scope of our article but should be an important subject for future research.

ACKNOWLEDGMENT

The work described in this article was carried out by the Jet Propulsion Laboratory, California Institute of Technology, under a contract with the National Aeronautics and Space Administration.

REFERENCES

- [1] D. Entekhabi *et al.*, “The soil moisture active passive (SMAP) mission,” *Proc. IEEE*, vol. 98, no. 5, pp. 704–716, May 2010.
- [2] Y. H. Kerr, P. Waldteufel, J.-P. Wigneron, J. Martinuzzi, J. Font, and M. Berger, “Soil moisture retrieval from space: The soil moisture and ocean salinity (SMOS) mission,” *IEEE Trans. Geosci. Remote Sens.*, vol. 39, no. 8, pp. 1729–1735, Aug. 2001.
- [3] M. Martin-Neira, “A passive reflectometry and interferometry system (PARIS): Application to ocean altimetry,” *ESA J.*, vol. 17, no. 4, pp. 331–355, 1993.
- [4] G. A. Hajj and C. Zuffada, “Theoretical description of a bistatic system for ocean altimetry using the GPS signal,” *Radio Sci.*, vol. 38, no. 5, pp. 10–19, Oct. 2003, doi: [10.1029/2002RS002787](https://doi.org/10.1029/2002RS002787).
- [5] V. U. Zavorotny, K. M. Larson, J. J. Braun, E. E. Small, E. D. Gutmann, and A. L. Bilich, “A physical model for GPS multipath caused by land reflections: Toward bare soil moisture retrievals,” *IEEE J. Sel. Topics Appl. Earth Observ. Remote Sens.*, vol. 3, no. 1, pp. 100–110, Mar. 2010, doi: [10.1109/JSTARS.2009.2033608](https://doi.org/10.1109/JSTARS.2009.2033608).
- [6] S. J. Katzberg, O. Torres, M. S. Grant, and D. Masters, “Utilizing calibrated GPS reflected signals to estimate soil reflectivity and dielectric constant: Results from SMEX02,” *Remote Sens. Environ.*, vol. 100, no. 1, pp. 17–28, 2006.
- [7] N. Rodriguez-Alvarez *et al.*, “Soil moisture retrieval using GNSS-R techniques: Experimental results over a bare soil field,” *IEEE Trans. Geosci. Remote Sens.*, vol. 47, no. 11, pp. 3616–3624, Nov. 2009, doi: [10.1109/TGRS.2009.2030672](https://doi.org/10.1109/TGRS.2009.2030672).
- [8] N. Rodriguez-Alvarez *et al.*, “Review of crop growth and soil moisture monitoring from a ground-based instrument implementing the interference pattern GNSS-R technique,” *Radio Sci.*, vol. 46, no. 6, pp. 1–11, Dec. 2011, doi: [10.1029/2011RS004680](https://doi.org/10.1029/2011RS004680).
- [9] N. Rodriguez-Alvarez *et al.*, “Land geophysical parameters retrieval using the interference pattern GNSS-R technique,” *IEEE Trans. Geosci. Remote Sens.*, vol. 49, no. 1, pp. 71–84, Jan. 2011, doi: [10.1109/TGRS.2010.2049023](https://doi.org/10.1109/TGRS.2010.2049023).
- [10] C. Ruf *et al.*, “New ocean winds satellite mission to probe hurricanes and tropical convection,” *Bull. Amer. Meteorol. Soc.*, vol. 97, pp. 385–395, 2016, doi: [10.1175/BAMS-D-14-00218.1](https://doi.org/10.1175/BAMS-D-14-00218.1).
- [11] A. Egido *et al.*, “Airborne GNSS-R polarimetric measurements for soil moisture and above-ground biomass estimation,” *IEEE J. Sel. Topics Appl. Earth Observ. Remote Sens.*, vol. 7, no. 5, pp. 1522–1532, May 2014.
- [12] C. Chew *et al.*, “Demonstrating soil moisture remote sensing with observations from the UK TechDemoSat-1 satellite mission,” *Geophys. Res. Lett.*, vol. 43, no. 7, pp. 3317–3324, 2016, doi: [10.1002/2016GL068189](https://doi.org/10.1002/2016GL068189).
- [13] A. Camps *et al.*, “Sensitivity of GNSS-R spaceborne observations to soil moisture and vegetation,” *IEEE J. Sel. Topics Appl. Earth Observ. Remote Sens.*, vol. 9, no. 10, pp. 4730–4742, Oct. 2016, doi: [10.1109/JSTARS.2016.2588467](https://doi.org/10.1109/JSTARS.2016.2588467).
- [14] A. Camps, M. Vall-llossera, H. Park, G. Portal, and L. Rossato, “Sensitivity of TDS-1 GNSS-R reflectivity to soil moisture: Global and regional differences and impact of different spatial scales,” *Remote Sens.*, vol. 10, no. 11, p. 1856, Nov. 2018, doi: [10.3390/rs10111856](https://doi.org/10.3390/rs10111856).
- [15] C. C. Chew and E. E. Small, “Soil moisture sensing using spaceborne GNSS reflections: Comparison of CYGNSS reflectivity to SMAP soil moisture,” *Geophys. Res. Lett.*, vol. 45, no. 9, pp. 4049–4057, May 2018, doi: [10.1029/2018GL077905](https://doi.org/10.1029/2018GL077905).
- [16] Chew, C. and E. Small. UCAR/CU CYGNSS Soil Moisture User Guide. Accessed: Apr. 1, 2019. [Online]. Available: <https://data.cosmic.ucar.edu/gnss-r/soilMoisture/cygnss/level3/>

- [17] H. Kim and V. Lakshmi, "Use of cyclone global navigation satellite system (CyGNSS) observations for estimation of soil moisture," *Geophys. Res. Lett.*, vol. 45, no. 16, pp. 8272–8282, Aug. 2018, doi: [10.1029/2018GL078923](https://doi.org/10.1029/2018GL078923).
- [18] M. P. Clarizia, N. Pierdicca, F. Costantini, and N. Flouri, "Analysis of CYGNSS data for soil moisture retrieval," *IEEE J. Sel. Topics Appl. Earth Observ. Remote Sens.*, vol. 12, no. 7, pp. 2227–2235, Jul. 2019.
- [19] O. Eroglu, M. Kurum, D. Boyd, and A. C. Gurbuz, "High spatio-temporal resolution CYGNSS soil moisture estimates using artificial neural networks," *Remote Sens.*, vol. 11, no. 19, p. 2272, Sep. 2019, doi: [10.3390/rs11192272](https://doi.org/10.3390/rs11192272).
- [20] M. M. Al-Khalidi, J. T. Johnson, A. J. O'Brien, A. Balenzano, and F. Mattia, Time-series retrieval of soil moisture using CYGNSS," *IEEE Trans. Geosci. Remote Sens.*, vol. 57, no. 7, pp. 4322–4331, Jul. 2019.
- [21] H. Carreno-Luengo, G. Luzi, and M. Crosetto, "Above-ground biomass retrieval over tropical forests: A novel GNSS-R approach with CyGNSS," *Remote Sens.*, vol. 12, no. 9, p. 1368, Apr. 2020.
- [22] X. Wu and S. Jin, "GNSS-Reflectometry: Forest canopies polarization scattering properties and modeling," *Adv. Space Res.*, vol. 54, no. 5, pp. 863–870, 2014.
- [23] N. Pierdicca, L. Guerriero, R. Giusto, M. Brogioni, A. Egido, "SAVERS: A simulator of GNSS reflections from bare and vegetated soils," *IEEE Trans. Geosci. Remote Sens.*, vol. 52, no. 10, pp. 6542–6554, Oct. 2014.
- [24] O. Eroglu, M. Kurum, and J. Ball, "Response of GNSS-R on dynamic vegetated terrain conditions," *IEEE J. Sel. Topics Appl. Earth Observ. Remote Sens.*, vol. 12, no. 5, pp. 1599–1611, May 2019, doi: [10.1109/JSTARS.2019.2910565](https://doi.org/10.1109/JSTARS.2019.2910565).
- [25] M. Kurum, M. Deshpande, A. T. Joseph, P. E. O'Neill, R. H. Lang, and O. Eroglu, "SCoBi-veg: A generalized bistatic scattering model of reflectometry from vegetation for signals of opportunity applications," *IEEE Trans. Geosci. Remote Sens.*, vol. 57, no. 2, pp. 1049–1068, Feb. 2019.
- [26] M. Zribi *et al.*, "Performance of GNSS-R GLORI data for biomass estimation over the Landes forest," *Int. J. Appl. Earth Observ. Geoinf.*, vol. 74, pp. 150–158, Feb. 2019.
- [27] V. L. Mironov, L. G. Kosolapova, and S. V. Fomin, "Physically and mineralogically based spectroscopic dielectric model for moist soils," *IEEE Trans. Geosci. Remote Sens.*, vol. 47, no. 7, pp. 2059–2070, Jul. 2009.
- [28] S. Gleason, C. Ruf, A. O'Brien, and D. McKague, "The CYGNSS level 1 calibration algorithm and error analysis based on on-orbit measurements," *IEEE J. Sel. Topics Appl. Earth Observ. Remote Sens.*, vol. 12, no. 1, pp. 37–49, Jan. 2019.
- [29] L. Tsang, J. A. Kong, and R. T. Shin, *Theory of Microwave Remote Sensing*. New York, NY, USA: Wiley, 1985.
- [30] R. D. De Roo and F. T. Ulaby, "Bistatic specular scattering from rough dielectric surfaces," *IEEE Trans. Antennas Propag.*, vol. 42, no. 2, pp. 220–231, Feb. 1994.
- [31] V. U. Zavorotny and A. G. Voronovich, "Scattering of GPS signals from the ocean with wind remote sensing application," *IEEE Trans. Geosci. Remote Sens.*, vol. 38, no. 2, pp. 951–964, Mar. 2000.
- [32] J. T. Johnson, K. F. Warnick, and P. Xu, "On the geometrical optics (Hagfors' Law) and physical optics approximations for scattering from exponentially correlated surfaces," *IEEE Trans. Geosci. Remote Sens.*, vol. 45, no. 8, pp. 2619–2629, Aug. 2007.
- [33] P. O'Neill, S. Chan, E. Njoku, T. Jackson, and R. Bindlish, "Soil moisture active passive (SMAP) algorithm theoretical basis document Level 2 & 3 soil moisture (passive) data products," Jet Propuls. Lab., California Inst. Technol., Pasadena, CA, USA, Tech. Rep. JPL E-66480, 2014.
- [34] J. Chaubell *et al.*, "Improving brightness temperature measurements near coastal areas for SMAP," *IEEE J. Sel. Topics Appl. Earth Observ. Remote Sens.*, vol. 12, no. 11, pp. 4578–4588, Nov. 2019, doi: [10.1109/JSTARS.2019.2951323](https://doi.org/10.1109/JSTARS.2019.2951323).
- [35] T. Jackson and T. J. Schmugge, "Vegetation effects on the microwave emission of soils," *Remote Sens. Environ.*, vol. 36, no. 3, pp. 203–212, 1991, doi: [10.1016/0034-4257\(91\)90057-D](https://doi.org/10.1016/0034-4257(91)90057-D).
- [36] H. Huang and L. A. S. Tsang Colliander Yueh, "Propagation of waves in randomly distributed cylinders using three-dimensional vector cylindrical wave expansions in Foldy-Lax equations," *IEEE J. Multiscale Multiphys. Comput. Techn.*, vol. 4, pp. 214–226, 2019.



Simon H. Yueh (Fellow, IEEE) received the Ph.D. degree in electrical engineering from the Massachusetts Institute of Technology, Cambridge, MA, USA, in January 1991.

He was a Post-Doctoral Research Associate with the Massachusetts Institute of Technology from February to August 1991. In September 1991, he joined Radar Science and Engineering Section, Jet Propulsion Laboratory (JPL), California Institute of Technology, Pasadena, CA, USA, where he has assumed various engineering and science management responsibilities. He served as a Project Scientist of the National Aeronautics and Space Administration (NASA) Aquarius Mission from January 2012 to September 2013 and a Deputy Project Scientist of the NASA Soil Moisture Active Passive (SMAP) Mission from January 2013 to September 2013. He has been serving as the SMAP Project Scientist since October 2013. He has been the Principal/Co-Investigator of numerous NASA and DOD research projects on remote sensing of ocean salinity, ocean wind, terrestrial snow, and soil moisture. He has authored four book chapters and published more than 200 publications and presentations.

Dr. Yueh is also a member of the American Geophysical Union and the URSI Commission F. He received the 2014 IEEE GRSS Transaction Prize Paper Award, the 2010 IEEE GRSS Transaction Prize Paper Award, the 2002 IEEE GRSS Transaction Prize Paper Award, the 2000 Best Paper Award at the IEEE International Geoscience and Remote Symposium 2000, and the 1995 IEEE GRSS Transaction Prize Paper Award for a paper on polarimetric radiometry. He also received the JPL Lew Allen Award in 1998, the JPL Ed Stone Award in 2003, the NASA Exceptional Technology Achievement Award in 2014, and the NASA Outstanding Public Leadership Medal in 2017. He was an Associate Editor of *Radio Science* from 2003 to 2007. He is also the Editor-in-Chief of the IEEE TRANSACTIONS ON GEOSCIENCE AND REMOTE SENSING.



Rashmi Shah (Senior Member, IEEE) received the B.S. degree in electrical engineering from the Rochester Institute of Technology, Rochester, NY, USA, in 2007, and the M.S. and Ph.D. degrees in aeronautical and astronautical engineering from Purdue University, West Lafayette, IN, USA, in 2010 and 2014, respectively.

Since 2014, she has been a Research Technologist with Tracking Systems and Applications Section, Jet Propulsion Laboratory (JPL), California Institute of Technology (Caltech), Pasadena, CA, USA. She is also a part of the core team member for JPL Foundry's A-team where she works with teams on early concept development. Her background and interests are microwave remote sensing, electromagnetic scattering, remote sensing using signals of opportunity reflectometry, and microwave remote sensing instrument development.

Dr. Shah was a recipient of the NASA Early Career Public Achievement Medal and the Institute of Electrical and Electronics Engineers (IEEE) Geoscience and Remote Sensing Society's (GRSS) Early Career Award. She also serves as the Co-Chair of the GNSS and Signals of Opportunity Working Group for the IEEE GRSS Society's Instrumentation and Future Technologies Technical Committee. She also serves as the Chapter Chair of the IEEE Metropolitan Los Angeles GRSS Chapter.



M. Julian Chaubell received the B.Sc. degree in mathematics from the National University of Mar del Plata, Buenos Aires, Argentina, in 1997, and the Ph.D. degree in applied and computational mathematics from the California Institute of Technology, Pasadena, CA, USA, in 2004, with a focus on low-coherence interferometric imaging.

In April 2004, he joined Jet Propulsion Laboratory (JPL), California Institute of Technology, as a Post-Doctoral Research Associate with the Tracking Systems and Applications Section, where he worked on the modeling of EM-wave propagation in fully 3-D atmospheric refractive index distributions. In April 2007, he joined the Radar Science and Engineering Section, JPL, as a permanent employee, where he has been working on the forward modeling of radar and radiometer measurements, as well as retrieval of the geophysical quantity from those measurements. He has also been involved in electromagnetic modeling of electrically large aperture systems and structures. He was part of the Soil Moisture Active Passive (SMAP) Instrument Operations Team and the SMAP Radar L1 Subsystem Team. He is also a part of the SMAP Radiometer L1 Team and the SMAP Soil Moisture L2 Team.



Akiko Hayashi received the B.S. degree in civil engineering and the M.S. degree in structural engineering from Duke University, Durham, NC, USA, in 1982 and 1984, respectively.

She is also a member of the Oceans and Ice Group, Jet Propulsion Laboratory (JPL), California Institute of Technology, Pasadena, CA, USA. After graduating in 1984, she came to JPL to work in the Structures and Dynamics Technology Group doing structural analysis and finite element modeling. In 1988, she moved to the Oceanography Group, where she started work on GEOSAT altimetry data. She is also working on projects with Jason-3, Aquarius, Soil Moisture Active Passive (SMAP), and CYGNSS satellites.



Xiaolan Xu (Member, IEEE) received the B.Eng. degree from Zhejiang University, Hangzhou, China, in 2006, and the M.S. and Ph.D. degrees in electrical engineering from the University of Washington, Seattle, WA, USA, in 2008 and 2011, respectively.

In 2012, she joined Jet Propulsion Laboratory (JPL), California Institute of Technology, Pasadena, CA, USA, as a Post-Doctoral Research Associate, where she became a Scientist in 2014. Her expertise is in the field of applied electromagnetics, electromagnetic wave propagation and scattering properties from snow-covered terrain, vegetated land surface and bare soil, forward modeling, and retrieval algorithm development with applications to Earth remote sensing in space.



Andreas Colliander (Senior Member, IEEE) received the M.Sc. (Tech.), Lic.Sc. (Tech.), and D.Sc. (Tech.) degrees from the Helsinki University of Technology (TKK; now Aalto University), Espoo, Finland, in 2002, 2005, and 2007, respectively.

He is also a Research Scientist with Jet Propulsion Laboratory, California Institute of Technology, Pasadena, CA, USA. His research is focused on the development of microwave remote sensing techniques. He is also leading the calibration and validation of the geophysical retrievals of NASA's Soil Moisture Active Passive (SMAP) Mission.